Dual-beam-scan Doppler optical coherence angiography for birefringence-artifact-free vasculature imaging

doi: 10.1364/OE.20.002681

Dual-beam-scan Doppler optical coherence angiography for birefringence-artifact-free vasculature imaging

Shuichi Makita, Franck Jaillon, Masahiro Yamanari, and Yoshiaki Yasuno*

Computational Optics Group in the University of Tsukuba, 1-1-1 Tennodai, Tsukuba, Ibaraki 305-8573, Japan

*yasuno@optlab2.bk.tsukuba.ac.jp

Abstract: Dual-beam-scan Doppler optical coherence angiography (DB-OCA) enables high-speed, high-sensitivity blood flow imaging. However, birefringence of biological tissues is an obstacle to vasculature imaging. Here, the influence of polarization and birefringence on DB-OCA imaging was analyzed. A DB-OCA system without birefringence artifact has been developed by introducing a Faraday rotator. The performance was confirmed *in vitro* using chicken muscle and *in vivo* using the human eye. Birefringence artifacts due to birefringent tissues were suppressed. Micro-vasculatures in the lamina cribrosa and nerve fiber layer of human eyes were visualized *in vivo*. High-speed and high-sensitivity micro-vasculature imaging involving birefringent tissues is available with polarization multiplexing DB-OCA.

OCIS codes: (110.4500) Optical coherence tomography; (170.3340) Laser Doppler velocimetry; (260.5430) Polarization; (170.4470) Ophthalmology.

References and links

1. W. Drexler and J. G. Fujimoto, eds., *Optical Coherence Tomography: Technology and Applications*, Biological and Medical Physics, Biomedical Engineering (Springer, 2008).
2. Z. Chen, T. E. Milner, S. Srinivas, X. Wang, A. Malekafzali, M. J. C. van Gemert, and J. S. Nelson, "Noninvasive imaging of *in vivo* blood flow velocity using optical Doppler tomography," Opt. Lett. **22**, 1119–1121 (1997).
3. J. A. Izatt, M. D. Kulkarni, S. Yazdanfar, J. K. Barton, and A. J. Welch, "*In vivo* bidirectional color Doppler flow imaging of picoliter blood volumes using optical coherence tomography," Opt. Lett. **22**, 1439–1441 (1997).
4. R. Leitgeb, L. Schmetterer, W. Drexler, A. Fercher, R. Zawadzki, and T. Bajraszewski, "Real-time assessment of retinal blood flow with ultrafast acquisition by color Doppler Fourier domain optical coherence tomography," Opt. Express **11**, 3116–3121 (2003).
5. B. R. White, M. C. Pierce, N. Nassif, B. Cense, B. H. Park, G. J. Tearney, B. E. Bouma, T. C. Chen, and J. F. de Boer, "*In vivo* dynamic human retinal blood flow imaging using ultra-high-speed spectral domain optical Doppler tomography," Opt. Express **11**, 3490–3497 (2003).
6. S. Makita, Y. Hong, M. Yamanari, T. Yatagai, and Y. Yasuno, "Optical coherence angiography," Opt. Express **14**, 7821–7840 (2006).
7. R. K. Wang and S. Hurst, "Mapping of cerebro-vascular blood perfusion in mice with skin and skull intact by optical micro-angiography at 1.3 μm wavelength," Opt. Express **15**, 11402–11412 (2007).
8. M. Szkulmowski, A. Szkulmowska, T. Bajraszewski, A. Kowalczyk, and M. Wojtkowski, "Flow velocity estimation using joint spectral and time domain optical coherence tomography," Opt. Express **16**, 6008–6025 (2008).
9. Y. K. Tao, A. M. Davis, and J. A. Izatt, "Single-pass volumetric bidirectional blood flow imaging spectral domain optical coherence tomography using a modified hilbert transform," Opt. Express **16**, 12350–12361 (2008).

#157816 - $15.00 USD Received 9 Nov 2011; revised 5 Jan 2012; accepted 9 Jan 2012; published 23 Jan 2012

10. B. J. Vakoc, R. M. Lanning, J. A. Tyrrell, T. P. Padera, L. A. Bartlett, T. Stylianopoulos, L. L. Munn, G. J. Tearney, D. Fukumura, R. K. Jain, and B. E. Bouma, "Three-dimensional microscopy of the tumor microenvironment *in vivo* using optical frequency domain imaging," Nat. Med. **15**, 1219–1223 (2009).
11. I. Grulkowski, I. Gorczynska, M. Szkulmowski, D. Szlag, A. Szkulmowska, R. A. Leitgeb, A. Kowalczyk, and M. Wojtkowski, "Scanning protocols dedicated to smart velocity ranging in spectral OCT," Opt. Express **17**, 23736–23754 (2009).
12. J. Fingler, R. J. Zawadzki, J. S. Werner, D. Schwartz, and S. E. Fraser, "Volumetric microvascular imaging of human retina using optical coherence tomography with a novel motion contrast technique," Opt. Express **17**, 22190–22200 (2009).
13. R. K. Wang, L. An, P. Francis, and D. J. Wilson, "Depth-resolved imaging of capillary networks in retina and choroid using ultrahigh sensitive optical microangiography," Opt. Lett. **35**, 1467–1469 (2010).
14. D. Y. Kim, J. Fingler, J. S. Werner, D. M. Schwartz, S. E. Fraser, and R. J. Zawadzki, "In vivo volumetric imaging of human retinal circulation with phase-variance optical coherence tomography," Biomed. Opt. Express **2**, 1504–1513 (2011).
15. S. Makita, F. Jaillon, M. Yamanari, M. Miura, and Y. Yasuno, "Comprehensive in vivo micro-vascular imaging of the human eye by dual-beam-scan Doppler optical coherence angiography," Opt. Express **19**, 1271–1283 (2011).
16. S. Zotter, M. Pircher, T. Torzicky, M. Bonesi, E. Götzinger, R. A. Leitgeb, and C. K. Hitzenberger, "Visualization of microvasculature by dual-beam phase-resolved Doppler optical coherence tomography," Opt. Express **19**, 1217–1227 (2011).
17. F. Jaillon, S. Makita, E. J. Min, B. H. Lee, and Y. Yasuno, "Enhanced imaging of choroidal vasculature by high-penetration and dual-velocity optical coherence angiography," Biomed. Opt. Express **2**, 1147–1158 (2011).
18. Q. Zhou and R. W. Knighton, "Light scattering and form birefringence of parallel cylindrical arrays that represent cellular organelles of the retinal nerve fiber layer," Appl. Opt. **36**, 2273–2285 (1997).
19. R. W. Knighton and X. R. Huang, "Linear birefringence of the central human cornea," Invest. Ophthalmol. Vis. Sci. **43**, 82–86 (2002).
20. J. T. Oh, S. W. Lee, Y. S. Kim, K. B. Suhr, and B. M. Kim, "Quantification of the wound healing using polarization-sensitive optical coherence tomography," J. Biomed. Opt. **11**, 041124 (2006).
21. S. Michels, M. Pircher, W. Geitzenauer, C. Simader, E. Gotzinger, O. Findl, U. Schmidt-Erfurth, and C. K. Hitzenberger, "Value of polarisation-sensitive optical coherence tomography in diseases affecting the retinal pigment epithelium," Br. J. Ophthalmol. **92**, 204–209 (2008).
22. M. Yamanari, S. Makita, V. Madjarova, T. Yatagai, and Y. Yasuno, "Fiber-based polarization-sensitive Fourier domain optical coherence tomography using B-scan-oriented polarization modulation method," Opt. Express **14**, 6502–6515 (2006).
23. S. Jiao and L. V. Wang, "Jones-matrix imaging of biological tissues with quadruple-channel optical coherence tomography," J. Biomed. Opt. **7**, 350–358 (2002).
24. Y. J. Hong, S. Makita, F. Jaillon, M. J. Ju, B. H. Lee, M. Itoh, M. Miura, and Y. Yasuno, Computational Optics Group in the University of Tsukuba, 1-1-1 Tennodai, Tsukuba, Ibaraki 305-8573, Japan, are preparing a manuscript to be called "High-penetration swept source Doppler optical coherence angiography by fully numerical phase stabilization."
25. A. Szkulmowska, M. Szkulmowski, A. Kowalczyk, and M. Wojtkowski, "Phase-resolved Doppler optical coherence tomography—limitations and improvements," Opt. Lett. **33**, 1425–1427 (2008).
26. A. L. Kornzweig, I. Eliasoph, and M. Feldstein, "Selective atrophy of the radial peripapillary capillaries in chronic glaucoma," Arch. Ophthalmol. **80**, 696–702 (1968).
27. M. Alterman and P. Henkind, "Radial peripapillary capillaries of the retina. II. Possible role in Bjerrum scotoma," Br. J. Ophthalmol. **52**, 26–31 (1968).
28. D. S. Greenfield, R. W. Knighton, and X. R. Huang, "Effect of corneal polarization axis on assessment of retinal nerve fiber layer thickness by scanning laser polarimetry," Am. J. Ophthalmol. **129**, 715–722 (2000).
29. C. K. Hitzenberger and A. F. Fercher, "Differential phase contrast in optical coherence tomography," Opt. Lett. **24**, 622–624 (1999).
30. D. P. Davé and T. E. Milner, "Optical low-coherence reflectometer for differential phase measurement," Opt. Lett. **25**, 227–229 (2000).
31. S. A. Telenkov, D. P. Dave, S. Sethuraman, T. Akkin, and T. E. Milner, "Differential phase optical coherence probe for depth-resolved detection of photothermal response in tissue," Phys. Med. Biol. **49**, 111–119 (2004).
32. S. Zotter, M. Pircher, E. Götzinger, T. Torzicky, M. Bonesi, and C. K. Hitzenberger, "Sample motion-insensitive, full-range, complex, spectral-domain optical-coherence tomography," Opt. Lett. **35**, 3913–3915 (2010).

1. Introduction

Optical coherence tomography (OCT) [1] enables high spatial resolution cross-sectional imaging. OCT is widely applied in several applications, especially in clinical ophthalmology. By using the phase of the OCT signal, micro-circulation inside of a tissue is measured and the vas-

#157816 - $15.00 USD Received 9 Nov 2011; revised 5 Jan 2012; accepted 9 Jan 2012; published 23 Jan 2012

culature is visualized [2–9]. Recently, several methods have demonstrated high-sensitivity in blood flow imaging by increasing the time separation of processed samples using smart scanning protocols [10, 11] or inter-frame processing [12–14] rather than inter-adjacent-axial-scan processing.

Other groups including the authors have used a two OCT signal detection approach at the same point but different time, with two OCT channels [15–17]. This method, so called dual-beam-scan Doppler optical coherence angiography (DB-OCA), potentially dissociates the measurable velocity range and the scanning protocol, and it easily enables simultaneous flow measurement using two different velocity ranges [17].

Despite these advantages of DB-OCA, there is a potential artifact in biological sample imaging. DB-OCA utilizes the phase shift between two OCT signals, which is detected by two isolated OCT channels. Polarization states at incident and/or detection arms differ between the two channels with regard to the polarization-multiplexing method [15, 17], and perhaps the dual-beam Doppler OCT method implemented with dual OCT systems [16] unless there is careful polarization control. The two OCT signals exhibit phase retardation when birefringent tissues are measured. The birefringence of biological tissues provides undesired phase shifts and obscures the flow signals.

Since birefringent tissues, for example collagen and fibril structure, are very common in biological samples and medical subjects [18–22], this artifact, which is caused by birefringence, will be problematic in extensive applications of DB-OCA. As the phase retardation due to birefringence will be accumulated as lights penetrating into tissues, the artifact will become prominent in regions behind thick and/or strong birefringent tissues, such as the nerve fiber layer and the lamina cribrosa in the eye.

In the present study, in order to eliminate this birefringence artifact, we introduced birefringence-artifact-free polarization multiplexing DB-OCA, by taking advantage of a polarization property of OCT measurement. Human eyes have been scanned *in vivo* to demonstrate the ability of this modality to image the micro-vasculature under birefringent tissues.

2. Methods

2.1. Principle of the dual-beam method

Before detailing the principle and the properties of our new DB-OCA method, we will briefly describe the principle of our old DB-OCA method. In the previous studies, the effect of the birefringence of the sample was ignored [15,17]. We re-formulated the principle of the old method, taking into consideration the sample birefringence. A schematic diagram of a probe arm used in the DB-OCA system is shown in Fig. 1. The dual-beam method uses two independent beams, which detect separate locations in the sample. The two beams are scanned for spatial sampling, and the following beam will reach a past sampling location of the preceding beam. There is a time-related phase change between the two signals at the same location sampled by each beam. The signals with two beams at the same location, **r**, can be expressed as:

$$\begin{cases} \Gamma_p(\mathbf{r},t) & = \mathbf{E}_{out}^{p\dagger}\mathbf{J}(\mathbf{r})\mathbf{E}_{in}^{p} \\ \Gamma_f(\mathbf{r},t+\Delta T) & = \mathbf{E}_{out}^{f\dagger}\mathbf{J}(\mathbf{r})\mathbf{E}_{in}^{f}e^{i\Delta\phi_m(\mathbf{r})} \end{cases}, \tag{1}$$

where Γ_p and Γ_f are OCT signals with p: preceding and f: following beams. E_{in} and E_{out} are Jones vectors that denote the incident and collecting polarization states of a probe beam. Superscripts of p and f express the preceding beam and the following beam. † is the conjugate transpose. **J** is the Jones matrix of the sample. $\Delta\phi_m$ is the phase shift introduced by the motion of the sample during the time separation ΔT.

#157816 - $15.00 USD Received 9 Nov 2011; revised 5 Jan 2012; accepted 9 Jan 2012; published 23 Jan 2012

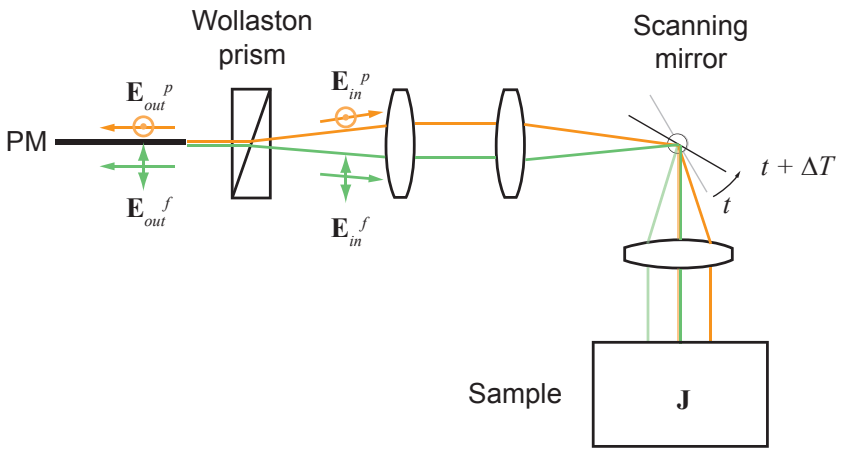

Fig. 1. Schematic diagram of probe arm in DB-OCA.

In OCT, the localized tissue information is carried by single scattered or least-scattered photons. These photons travel forward and backward along almost the same path. The polarization properties of samples can be expressed as the Jones matrix $\mathbf{J}$=$\mathbf{J}_s^T\mathbf{J}_s$, where $\mathbf{J}_s$ is the single-trip Jones matrix of the sample, and it is transpose symmetric [23]:

$$\mathbf{J} = \begin{bmatrix} j_{11} & j_{12} \\ j_{21} & j_{22} \end{bmatrix}, \ (j_{12} \equiv j_{21}). \tag{2}$$

In the polarization-multiplexing dual-beam method, the incident and detected polarization states are linear polarization states, and they are parallel to each other while the two channels are perpendicular to each other. Here, polarization states for each channel are assumed to be $\mathbf{E}_{in}^{p} \parallel \mathbf{E}_{out}^{p} \parallel [1\ 0]^T$ and $\mathbf{E}_{in}^{f} \parallel \mathbf{E}_{out}^{f} \parallel [0\ 1]^T$. By substituting Eq. (2) and polarization states in Eq. (1), OCT signals are

$$\begin{cases} \Gamma_p(\mathbf{r},t) & \propto j_{11}(\mathbf{r}) \\ \Gamma_f(\mathbf{r},t+\Delta T) & \propto j_{22}(\mathbf{r})e^{i\phi_m(\mathbf{r})} \end{cases}. \tag{3}$$

The motion of the sample was estimated by calculating the phase difference between the two OCT signals as:

$$\Delta\phi(\mathbf{r}) = Arg[\Gamma_f(\mathbf{r})\Gamma_p^*(\mathbf{r})] = \Delta\phi_m(\mathbf{r}) + \Delta\phi_b(\mathbf{r}), \tag{4}$$

where $\Delta\phi_b$ is the phase shift due to the sample birefringence and equals $\angle j_{22} - \angle j_{11}$ when Eq. (3) is true. We should note that the $\Delta\phi_b$ evidently disturbs the motion estimation.

2.2. Dual-beam OCA without birefringence artifact

The schematic diagram of the newly developed DB-OCA system that is free from birefringence artifact is shown in Fig. 2. The probe arm has been modified from the previously reported DB-OCA system based on a 840-nm wavelength [15]. The Faraday rotator (WT-04-R-850: EOT, Michigan, USA) was introduced after the Wollaston prism. The relay lens pair conjugates the dividing point between the two beams and the pivot point of the fast-scanning galvanometer mirror. This condition was designed to achieve the same incident angle of two beams, at the same sampling location on the sample. As a result, the illumination area completely overlaps even at the out-of-focus plane. An achromatic quarter wave plate (AQWP05M-950: Thorlabs, New Jersey, USA) was placed before the galvanometer scanner unit.

#157816 - $15.00 USD Received 9 Nov 2011; revised 5 Jan 2012; accepted 9 Jan 2012; published 23 Jan 2012

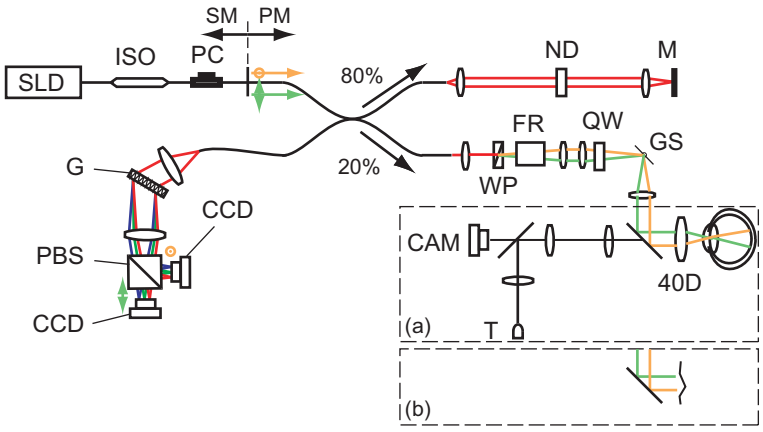

Fig. 2. The schematic diagram of the birefringence artifact free dual-beam-scan Doppler optical coherence angiography system. SM, PM: single-mode and polarization-maintaining fiber; ISO: isolator; WP: Wollaston prism; FR: Faraday rotator; QW: quarter wave plate; PC: polarization controller; G: grating; PBS: polarization beam splitter; CCD: line-scan CCD camera; CAM: 2D camera for pupil monitor; T: laser emission diode for fixation.

The probe arm is switched according to the samples, i.e. for posterior eye imaging (a) and for non posterior eye imaging (b). For *in vivo* human eye imaging, the pupil monitor and fixation target (green LED) are involved for aiming the probing beams and to stabilize gaze. For each configuration, the beam spot diameters on samples were 13 and 11 μm (FWHM: full-width at half-maximum).

Two CCD cameras in the polarization-sensitive spectrometer were synchronized and driven at the acquisition rate of 27,778 lines/s. The integration time was 34.8 μs.

2.2.1. Principle of birefringence artifact removal

To avoid the birefringence artifact, the Faraday rotator with 45 degrees rotation and the quarter wave plate were introduced after the Wollaston prism. The Jones matrix of the combination of the sample, Faraday rotator and quarter wave plate can be expressed as:

$$\begin{aligned}\mathbf{M} &= \mathbf{R}(\pi/4)\mathbf{Q}^T(0)\mathbf{J}\mathbf{Q}(0)\mathbf{R}(\pi/4) \\ &= \frac{i}{2}\begin{bmatrix} j_{11}+j_{22} & j_{11}-i2j_{12}-j_{22} \\ -j_{11}-i2j_{12}+j_{22} & -(j_{11}+j_{22}) \end{bmatrix},\end{aligned} \tag{5}$$

where $\mathbf{R}$ is a rotation matrix used to express the Faraday rotation and $\mathbf{Q}$ is the Jones matrix of a quarter wave plate. Here, the optic axis of the quarter wave plate was assumed to be aligned vertically. It does not matter whether it is a slow or fast axis. In both cases, the effect is the same. Note that the diagonal elements of the matrix $\mathbf{M}$ differ only in their signs. Under this condition, Eq. (1) can be re-written as

$$\begin{cases}\Gamma_p(\mathbf{r},t) & = \mathbf{E}_{out}^{p\dagger}\mathbf{M}(\mathbf{r})\mathbf{E}_{in}^{p} \\ \Gamma_f(\mathbf{r},t+\Delta T) & = \mathbf{E}_{out}^{f\dagger}\mathbf{M}(\mathbf{r})\mathbf{E}_{in}^{f}e^{i\Delta\phi_m(\mathbf{r})}\end{cases}. \tag{6}$$

Because of the polarization-multiplexing scheme, polarization states for each channel are, $\mathbf{E}_{in}^{p} \parallel \mathbf{E}_{out}^{p} \parallel [1\ 0]^T$ and $\mathbf{E}_{in}^{f} \parallel \mathbf{E}_{out}^{f} \parallel [0\ 1]^T$. By substituting Eq. (5) into Eq. (6) and considering the

#157816 - $15.00 USD Received 9 Nov 2011; revised 5 Jan 2012; accepted 9 Jan 2012; published 23 Jan 2012

polarization states, the OCT signals become

$$\begin{cases} \Gamma_p(\mathbf{r},t) & \propto \frac{i}{2}[j_{11}(\mathbf{r})+j_{22}(\mathbf{r})] \\ \Gamma_f(\mathbf{r},t+\Delta T) & \propto -\frac{i}{2}[j_{11}(\mathbf{r})+j_{22}(\mathbf{r})]e^{i\phi_m(\mathbf{r})} \end{cases}. \tag{7}$$

The phase shift between the two channels is then calculated as:

$$\Delta\phi(\mathbf{r}) = Arg[\Gamma_f(\mathbf{r})\Gamma_p^*(\mathbf{r})] = \Delta\phi_m(\mathbf{r}) + \pi. \tag{8}$$

It can then be found that the birefringence artifact term that appeared in Eq. (4) is eliminated. Although there is the constant phase error π on the right side of Eq. (8), this error can be canceled when we apply bulk motion compensation methods [6,24]. The birefringence-artifact-free motion imaging is available.

In this scheme, non-reciprocal polarization rotation by a Faraday rotator is the essence of birefringence artifact removal. The function of the quarter wave plate following the Faraday rotator is only to optimize the probe power efficiency. The 45° non-reciprocal rotation and transpose symmetry of a round-trip Jones matrix of elements followed by the Faraday rotator ($\mathbf{Q}^T\mathbf{JQ}$) result in a constant phase shift (π) between the diagonal elements of a Jones matrix of entire probe arm $\mathbf{M}$. Hence, birefringence artifacts can be eliminated in spite of any polarization element (except non-reciprocal one) following the Faraday rotator.

The quarter wave plate was introduced to compensate for the signal collection efficiency. If there is no quarter wave plate and no birefringence of samples, signal powers, $|\Gamma_p|^2$ and $|\Gamma_f|^2$, will be zero. Both structure and flow images cannot be obtained. A quarter wave plate is the optimum compensator to maximize the signal collection efficiency with non-birefringent samples. When we assume that the sample is a linear phase retarder, its Jones matrix $\mathbf{J}$ is

$$j_{11,22} = \cos\frac{\delta}{2} \pm i\cos 2\theta \sin\frac{\delta}{2} \tag{9}$$

where δ is phase retardation and θ is the orientation of the sample's optic axis. This is a reasonable assumption for normal biological samples. By substituting Eq. (9) into Eq. (7), the signal power can be described as

$$|\Gamma_{p\ or\ f}|^2 \propto \cos^2\frac{\delta}{2}. \tag{10}$$

Apparently, Eq. (10) is the maximum when $\delta = 0$.

3. Results

3.1. Evaluation using birefringent tissues

The performance of birefringence artifact removal was demonstrated by means of birefringent samples, and the results were compared with those of the previous scheme that did not involve birefringence artifact removal (Sec. 2.2.1 & Ref. [15]). Chicken muscle was used as the birefringent sample. The ophthalmic lens was removed to enable the placement of the sample in the probe arm (Fig. 2(b)). The measurement was carried out twice with and without the Faraday rotator and the quarter wave plate. The scanning range was 2 mm, and 100 B-scans consisting of 512 lines were acquired within 2.1 s. The time separation between two probing beams was 1.58 ms. Figure 3 shows a single frame of intensity and phase-resolved images for each measurement. Since this was an *ex vivo* measurement and blood flow does not exist, if it was not random phase noise, the Doppler signals observed with this sample were a birefringence artifact. The phase difference without the Faraday rotator and quarter wave plate showed prominent birefringence artifacts (Fig. 3(b)). On the other hand, the artifacts were significantly reduced in

#157816 - $15.00 USD Received 9 Nov 2011; revised 5 Jan 2012; accepted 9 Jan 2012; published 23 Jan 2012

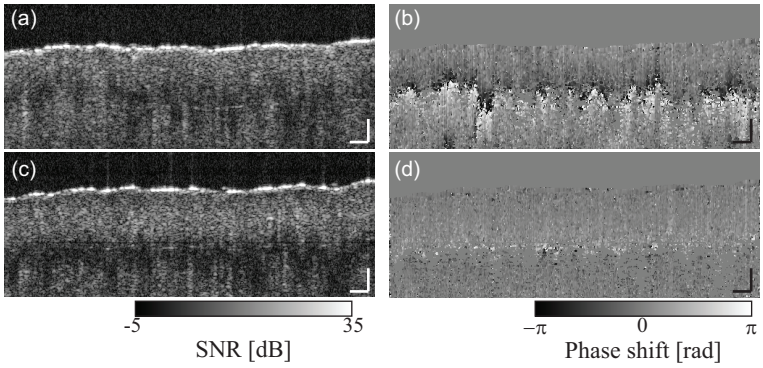

Fig. 3. Chicken muscle images (a, b) without and (c, d) with birefringence artifact removal. Cross-sectional morphology (a, c) and phase differences (b, d) are shown. The scan range is 2 mm (512 lines). Scale bars indicates 100 μm.

the system with the Faraday rotator and quarter wave plate (Fig. 3(d)). The average phase shift under 150 μm depth from the surface were calculated using the circular mean [25] (512 $\times$ 100 = 51,200 points). The average phase shifts were 0.282 and -0.631 radians with and without birefringence artifact removal, respectively. The magnitude of the phase error was reduced by more than a factor of two. Unfortunately, the artifacts were not completely removed. Perhaps this was due to the non-ideal Faraday rotation angle. The discrepancy from 45-degree rotation and wavelength-dependent rotation would have caused the residual artifacts.

3.2. In vivo human eye imaging

In the case of the human eye, some birefringent tissues such as the nerve fiber, the lamina cribrosa and the cornea would affect the dual-beam-scan flow imaging. The micro-vasculature around the optic nerve head (ONH) in several healthy eyes has been scanned. The scanning range was 2 $\times$ 2 mm^2 (512 $\times$ 256 lines) were detected within 5.4 s. The time separation between two probing beams was 1.58 ms. In some eyes, the quarter wave plate in the sample arm was rotated to suppress the residual birefringence artifacts by monitoring phase-resolved flow image. The details are discussed at the Sec. 4.1.

The comparison of the vasculature images with and without birefringence artifact removal is shown in Fig. 4. The same eye has been scanned with both configurations. The projection images of squared Doppler phase shifts visualized vasculature superior to the ONH and the optic disc regions. Since the birefringence artifacts were significant, the vasculature was disturbed (Fig. 4(a)) or in some parts completely obscured (Fig. 4(c)) without artifact removal. With birefringence artifact removal configuration, retinal and choroidal vessels (Fig. 4(b)) and vasculature in the optic disc (Fig. 4(d)) were visualized in high contrast (e.g., regions indicated as blue arrows in Fig. 4).

Comparison of OCT cross sections showed that a comparable signal intensity was achieved with the birefringence artifact scheme (Figs. 5(a) and (d)). Cross-sectional blood flow images exhibited a strong artifact at the lamina cribrosa (Figs. 5(b) and (c)). In addition, the region above the lamina cribrosa had artifacts that appeared as some vertical lines. These resulted from the failure of bulk motion compensation. The bulk motion was estimated by means of a mode of phase change in the single axial profile, and was subtracted from the original phase shift axial profile [6]. When there is prominent birefringence artifacts in the lamina cribrosa, the bulk motion estimation will fail and an incorrect bulk motion correction will be applied to an entire axial profile. Hence, this shows that birefringence artifacts do not only disturb the

#157816 - $15.00 USD Received 9 Nov 2011; revised 5 Jan 2012; accepted 9 Jan 2012; published 23 Jan 2012

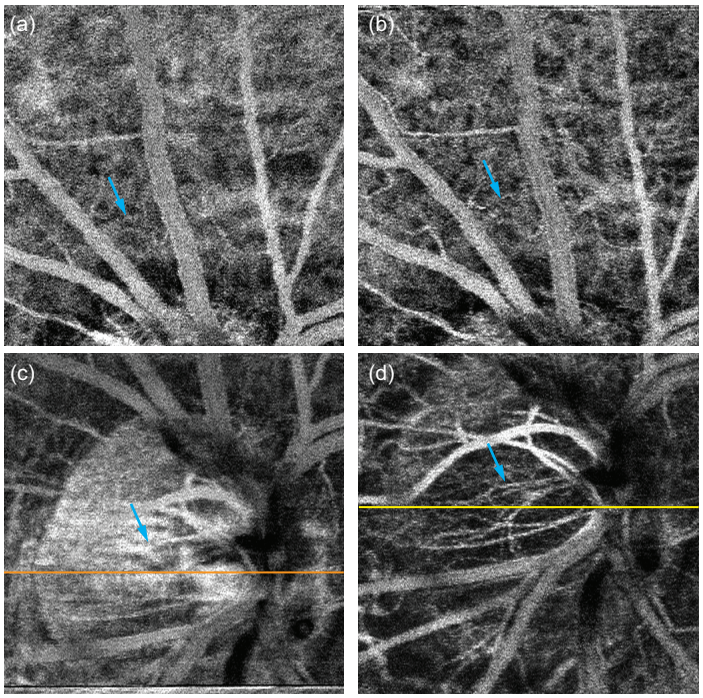

Fig. 4. Vasculature *in vivo* images of human eye obtained using DB-OCA (a, c) without and (b, d) with birefringence artifact removal. The images were obtained in the same eye. The orange (c) and yellow (d) lines indicate the location of cross-sectional images in Fig. 5.

vasculature in and below the birefringence tissue, but also in some regions above these tissues. These artifacts were removed using the birefringence artifact removal scheme (Figs. 5(e) and (f)). Some flow signals are shown in large retinal vessels and the lamina cribrosa.

Depth-resolved vasculature imaging at the ONH showed micro-vasculature in the optic disc of two subjects (Figs. 6(a) and (c)). The axial locations of vessels are coded in colors as shown in Figs. 6(b) and (d). The vasculatures extending from the prelaminar region (yellow) to the lamina cribrosa (purple) were observed.

In the peripapillary region without birefringence artifact removal, the thick nerve fiber layer could cause strong phase retardation. However, this is not apparent in Fig. 7. In the superficial region of the retinal nerve fiber layer, radially running fine vessels from the optic disc are shown (Figs. 7(a) and (c)). These are radial peripapillary capillaries that nourish the thick retinal nerve fiber layer. The property of this vasculature is known to be related to some optic neuropathies such as glaucoma [26, 27]. The vasculature in the plexiform layers and the nuclear layers is shown in Figs. 7(b) and (d). The complex retinal capillary network and thick retinal vessels can be observed.

4. Discussion

4.1. Residual birefringence artifact

In some eyes evaluated in our study, the vasculature imaging at the ONH exhibited prominent residual birefringence artifacts in and/or beneath the lamina cribrosa. Two of 4 eyes exhibited significant residual artifacts. Both are myopia and the others are emmetropia. Perhaps this was due to the non-ideal rotation angle of our Faraday rotator. The effect of imperfect Faraday

#157816 - $15.00 USD Received 9 Nov 2011; revised 5 Jan 2012; accepted 9 Jan 2012; published 23 Jan 2012

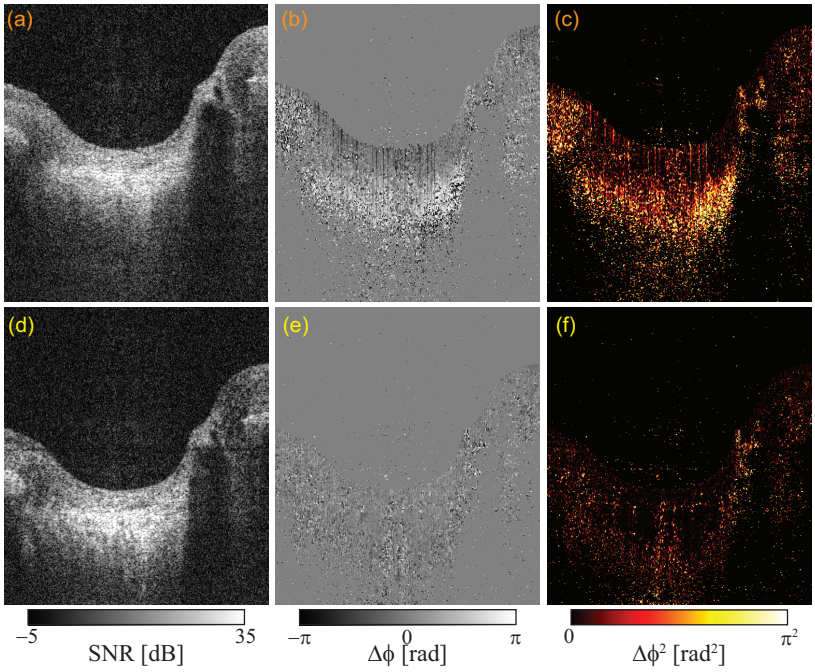

Fig. 5. Cross-sectional DB-OCA images (a,b,c) without and (d,e,f) with birefringence artifact removal at the ONH indicated in Figs. 4(c) and (d). (a,d) OCT, (b,e) bi-directional Doppler and (c,f) squared Doppler flow images.

rotation on birefringence artifact removal has been analyzed by introducing an error in the Faraday rotation, say σ, into Eq. (5) and substituting to Eq. (6), then the phase shift between two OCT signals was calculated numerically. The result is shown in Fig. 8, where δ and θ are the round-trip phase retardation and the optic axis orientation of a linear retarder sample. The numerical simulation showed that there would be high residual birefringence artifacts when phase retardation is large ($\delta \sim \pm\pi$), and its amount would depend on the sample orientation. This finding can reasonably explain the variation in the experiments. Since the signal from the lamina cribrosa will be affected by the polarization properties of the lamina and cornea, which are varied among subjects [28], the cumulative phase retardation distribution and the cumulative optic axis orientation in the lamina cribrosa will differ between individuals.

During the imaging of some eyes, it was found that the residual birefringence artifact was suppressed by rotating the quarter wave plate in the probe arm. This can be expressed by the following assumption. The Jones matrix of the probe arm with non-ideal Faraday rotation and variable orientation of the quarter wave plate can be written as:

$$\mathbf{M}' = \mathbf{R}(\pi/4+\sigma)\mathbf{Q}^T(\psi)\mathbf{J}\mathbf{Q}(\psi)\mathbf{R}(\pi/4+\sigma) \tag{11}$$

where σ is the deviation in the Faraday rotation angle from the ideal value $\pi/4$, and ψ is the orientation of the quarter wave plate. When the phase difference between the diagonal elements in Eq. (11) was constant, the birefringence artifact disappeared. Assume that the sample is a linear phase retarder, and the condition, $M'_{11} = -M'_{22}$, which is equivalent to the ideal case (Eq. (5)) is true. Then it can be expected that the birefringence artifact would be canceled when the orientation of the quarter wave plate meets the condition

$$\psi = \theta \pm \frac{\pi}{4}. \tag{12}$$

#157816 - $15.00 USD Received 9 Nov 2011; revised 5 Jan 2012; accepted 9 Jan 2012; published 23 Jan 2012

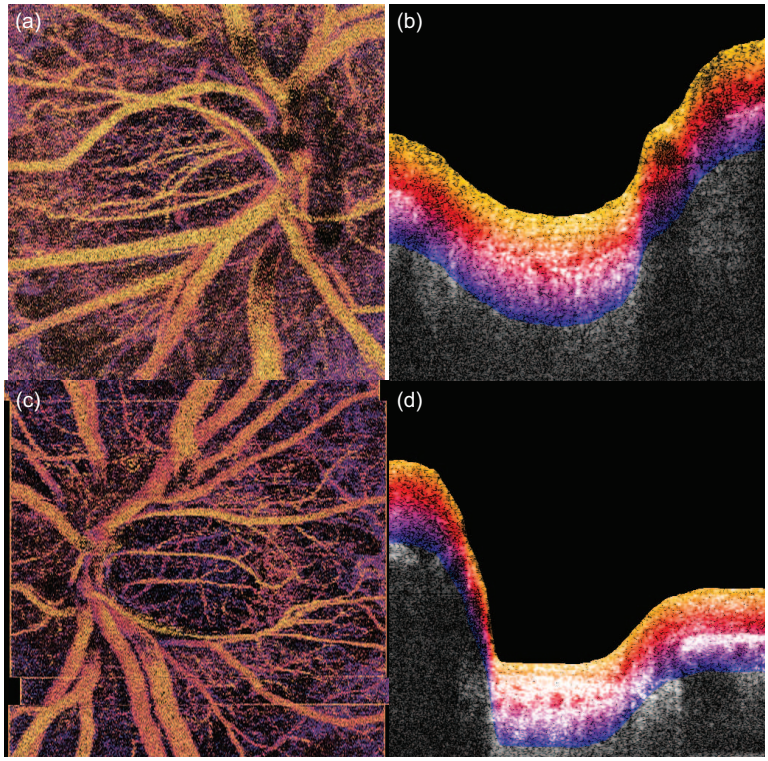

Fig. 6. Depth-resolved vasculature images at the ONH ((a) and (c)). The color table assigned for the depth is shown in OCT cross sections ((b) and (d)).

Note that this condition (Eq. (12)) is satisfied at the specific locations where the sample orientation is θ. The other locations that exhibited different orientations were not in the condition, and the residual birefringence artifact could be apparent. In Sec. 2.2.1, the orientation of the quarter wave plate was determined only for optimizing of the signal collection efficiency. Here, the orientation was shifted to reduce the residual birefringence artifact. The discrepancy will cause only signal power loss and no additional artifact.

4.2. Signal power compensation for in vivo eye imaging

There is another reason for rotating the quarter wave plate. The orientation of the quarter wave plate was optimized to achieve the maximum signal power with non-birefringent tissues (in Sec. 2.2.1); however, it was not optimum in the case of *in vivo* human eye imaging. Since the light passes through the anterior part of the eye to reach the posterior part, the birefringence of tissues in the anterior region, especially the cornea, alters the polarization states and reduces the signal power efficiency. The orientation of the quarter wave plate should be optimized for each individual eye.

4.3. Birefringence artifact in interferometer-multiplexing method

In the present study, we demonstrated birefringence artifact removal in polarization-multiplexing DB-OCA. On the other hand, there is another method by using two independent interferometers [16]. Even for this interferometer-multiplexing method, the birefringence of the sample results in uncontrolled phase offset between two OCT signals and generates birefrin-

#157816 - $15.00 USD Received 9 Nov 2011; revised 5 Jan 2012; accepted 9 Jan 2012; published 23 Jan 2012

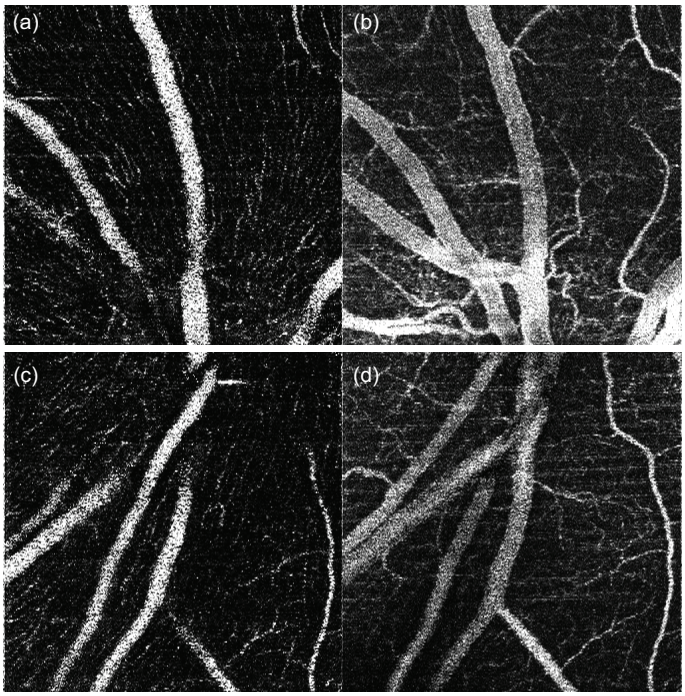

Fig. 7. Depth discriminated vasculature images in the peripapillary region. (a, c) Superficial retinal nerve fiber layer ($\sim 62\ \mu$m thick from the surface); (b, d) from inner plexiform layer to outer nuclear layers. The superior (a, b) and inferior (c, d) to the ONH are shown.

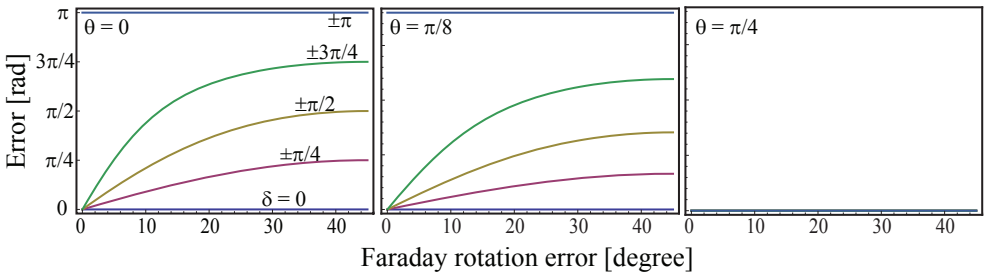

Fig. 8. Numerical simulation result for birefringence artifact removal error due to imperfect Faraday rotation. δ and θ are the round-trip phase retardation and the optic axis orientation of a sample.

#157816 - $15.00 USD Received 9 Nov 2011; revised 5 Jan 2012; accepted 9 Jan 2012; published 23 Jan 2012

gence artifact.

One solution is, as expected from Eqs. (1) and (4), usage of the identical polarization state for two incident lights and the identical detection state, i.e. $\mathbf{E}_{in}^{p} \parallel \mathbf{E}_{in}^{f}$ and $\mathbf{E}_{out}^{p} \parallel \mathbf{E}_{out}^{f}$, where the detection states $\mathbf{E}_{out}^{p}$ and $\mathbf{E}_{out}^{f}$ are corresponding to polarization states of reference beams in the interferometer-multiplexing method. In order to fulfill this condition, the polarization of two interferometers should be carefully controlled to have identical probe and reference states.

4.4. Applications for other methods

There are other methods that apply a similar detection scheme with two OCT channels and a phase difference between them, such as differential phase contrast imaging [29–31] and phase-resolved measurement between two OCT signals [32]. This birefringence artifact removal scheme will also be available for these methods.

5. Conclusion

In the present study, the birefringence artifact, which is a significant obstacle for DB-OCA imaging, was eliminated by introducing Faraday rotation. The signal efficiency was compensated for by a wave plate. Birefringence-artifact-free polarization-multiplexing DB-OCA was performed to visualize the micro-vasculature in birefringent tissues. Fine vessels in the lamina cribrosa, in the thick nerve fiber layer and underneath the nerve fiber layer of the human eye *in vivo* have been observed. The availability of high-speed and high-sensitivity vasculature imaging in birefringent tissues will extend the application fields of DB-OCA.

Acknowledgments

This research was partially supported by the Japan Science and Technology Agency through the contract of Development of Systems and Technology for Advanced Measurement and Analysis.

#157816 - $15.00 USD Received 9 Nov 2011; revised 5 Jan 2012; accepted 9 Jan 2012; published 23 Jan 2012